

Brushlets: A Tool for Directional Image Analysis and Image Compression

François G. Meyer¹ and Ronald R. Coifman

Department of Mathematics, Yale University, 12 Hillhouse Avenue, New Haven, Connecticut 06520

Communicated by Jelena Kovacevic

Received June 14, 1996; revised December 24, 1996

We construct a new adaptive basis of functions which is reasonably well localized with only one peak in frequency. We develop a compression algorithm that exploits this basis to obtain the most economical representation of the image in terms of textured patterns with different orientations, frequencies, sizes, and positions. The technique directly works in the Fourier domain and has potential applications for compression of highly textured images, texture analysis, etc. © 1997 Academic Press

I. INTRODUCTION

Edges and textures in an image can exist at all possible locations, orientations, and scales. The ability to efficiently analyze and describe textured patterns is thus of fundamental importance for image analysis and image compression. Wavelets provide an octave based decomposition of the Fourier plane with a poor angular resolution. Wavelet packets make it possible to adaptively construct an optimal tiling of the Fourier plane, and they have been used for image compression [1]. However the tensor product of two real valued wavelet packets is always associated with four symmetric peaks in the frequency plane. It is therefore not possible to selectively localize a unique frequency. Directionally oriented filter banks [2] have been used for image compression and image analysis. However they do not allow an arbitrary partitioning of the Fourier plane. Steerable filters with arbitrary orientation have been designed in [3]. However, these filters are significantly overcomplete: the number of coefficients is increased by more than $5^{\frac{1}{3}}$; this is serious drawback for image compression. Furthermore, these filters are not orthogonal, and therefore there is no efficient algorithm to adaptively select the best set of filters that is needed to describe an image.

In order to obtain a better angular resolution than the standard wavelet packets we expand the Fourier plane into windowed Fourier bases [4]. The method results in an

¹ E-mail: francois.meyer@yale.edu.

expansion of the image into a set of *brushlets*. A brushlet is a function reasonably well localized with only one peak in frequency. Furthermore, the brushlet is a complex valued function with a phase. The phase of the bi-dimensional brushlet provides valuable information about the orientation of the brushlet. We can adaptively select the size and locations of the brushlets in order to obtain the most concise and precise representation of an image in terms of oriented textures with all possible directions, frequencies, and locations. We demonstrate that this new basis can be used for directional image analysis and to efficiently compress richly textured images.

This paper is organized as follows. In the next section we review the construction of orthonormal windowed Fourier bases. This is followed in section III by a description of biorthogonal windowed Fourier bases. The new brushlet basis is given in section IV. A biorthogonal brushlet basis is presented in section V. In section VI we describe the image compression algorithm based on a brushlet expansion of the image. Results of experiments are presented in Section VII.

II. ORTHONORMAL WINDOWED FOURIER BASES

We are interested in a local “time frequency” analysis of the Fourier transform of a signal. We explain here how to perform a time-frequency analysis with windowed Fourier bases. In order to analyze the local frequency content of a signal, we first cut the support of the signal into adjacent intervals. Then a local Fourier analysis is performed inside each interval. To obtain a better frequency localization, we do not cut abruptly the signal, but we use a smooth window function to localize the segment of interest. We want to construct orthonormal bases with good “time-frequency” localization. We know from the Ballian-Low theorem [5] that we cannot use windowed exponentials of the form

$$g_{n,m}(x) = e^{im\omega_0 x} g(x - nt_0). \quad (1)$$

In order to circumvent the obstacle raised by the Ballian-Low theorem various Wilson bases have been constructed that use sines and cosines rather than exponential [6], [7], [8]. We are interested in using exponentials, because the phase of the exponential will provide information about the direction of the pattern when describing images in two dimensions. Therefore we will use the construction described in [4], and more precisely we will use the *smooth local periodization* technique introduced in [4]. The technique permits us to expand a function restricted to an interval into a periodic basis (such as exponentials) without creating any discontinuities at the endpoints of the interval. Conversely, we can construct smooth compactly supported orthonormal bases from periodic bases such as exponential functions.

First we review the construction of smooth localized orthonormal exponential bases [4], [9]. These functions are exponentials with good localization in both position and Fourier space. We consider a cover $\mathbb{R} = \bigcup_{n=-\infty}^{n=+\infty} [a_n, a_{n+1}]$. We write $l_n = a_{n+1} - a_n$, and $c_n = (a_n + a_{n+1})/2$. Around each a_n we define a neighborhood of radius ϵ . Let r be a ramp function such that

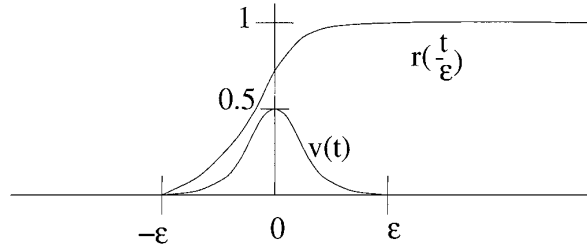


FIG. 1. Ramp function r and bump function v .

$$r(t) = \begin{cases} 0 & \text{if } t \leq -1 \\ 1 & \text{if } t \geq 1 \end{cases} \quad (2)$$

and

$$r^2(t) + r^2(-t) = 1, \quad \forall t \in \mathbb{R}. \quad (3)$$

Let v be the bump function supported on $[-\epsilon, \epsilon]$ (see Fig. 1)

$$v(t) = r\left(\frac{t}{\epsilon}\right)r\left(-\frac{t}{\epsilon}\right). \quad (4)$$

Let b_n be the windowing function supported on $[-l_n/2 - \epsilon, l_n/2 + \epsilon]$ (see Fig. 2)

$$\begin{aligned} b_n(t) &= r^2\left(\frac{t + l_n/2}{\epsilon}\right) && \text{if } t \in [-l_n/2 - \epsilon, -l_n/2 + \epsilon] \\ &= 1 && \text{if } t \in [-l_n/2 + \epsilon, l_n/2 - \epsilon] \\ &= r^2\left(\frac{l_n/2 - t}{\epsilon}\right) && \text{if } t \in [l_n/2 - \epsilon, l_n/2 + \epsilon]. \end{aligned} \quad (5)$$

We consider the collection of exponential functions

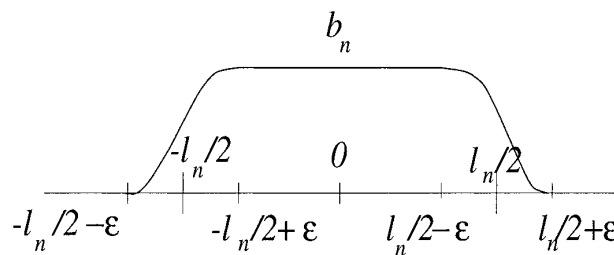


FIG. 2. Windowing function b_n .

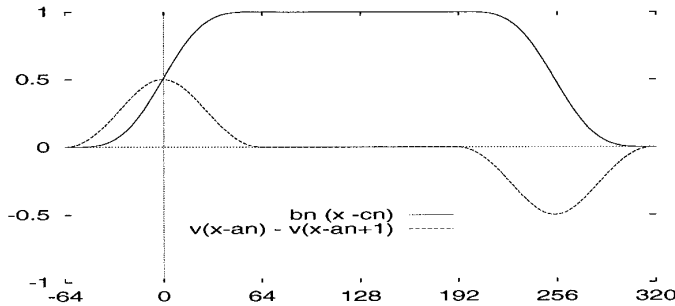


FIG. 3. Windowing function b_n and bump function v at both ends of the interval $[0, 256]$, with $\epsilon = 64$.

$$e_{j,n} = \frac{1}{\sqrt{l_n}} e^{-2i\pi j((x-a_n)/l_n)}.$$

We can construct a basis of smooth localized orthonormal exponential functions $u_{j,n}$, where each $u_{j,n}$ is supported on $[a_n - \epsilon, a_{n+1} + \epsilon]$ and is given by [9]

$$u_{j,n}(x) = b_n(x - c_n)e_{j,n}(x) + v(x - a_n)e_{j,n}(2a_n - x) - v(x - a_{n+1})e_{j,n}(2a_{n+1} - x) \quad (6)$$

(Fig. 4). If we consider all the $u_{j,n}$ associated with all the intervals $[a_n, a_{n+1}]$ we obtain an orthonormal basis of $L^2(\mathbb{R})$ [4, 9]:

THEOREM 1 [4, 9]. *The collection $\{u_{j,n}, n \in \mathbb{Z}\}$ is an orthonormal basis for $L^2(\mathbb{R})$.*

We note that this basis uses exponentials; other smooth local bases that use sines or cosines only can be constructed also [8]. Figure 4 shows the real and imaginary parts of the function $u_{j,n}$ with $a_n = 0$, $a_{n+1} = 256$, $l_n = 256$, and $j = 5$. We note in Fig. 4 that $u_{j,n}$ is locally even around a_n and locally odd around a_{n+1} . For this reason, the inner product of two contiguous basis functions $u_{j,n}$ and $u_{j,n+1}$ will be zero.

A. Implementation by Folding

In practice, in order to expand a function f into the basis $u_{j,n}$ we do not calculate the correlation between f and the basis $\{u_{j,n}\}$. Instead, we transform f restricted to

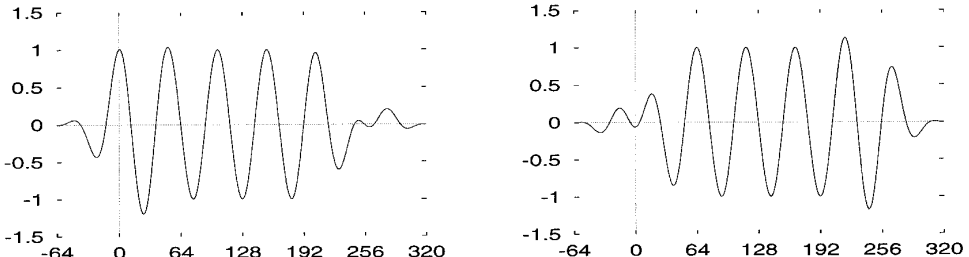


FIG. 4. Real (left) and imaginary (right) parts of the windowed exponential function $u_{j,n}$, with $a_n = 0$, $a_{n+1} = 256$, and $\epsilon = 64$.

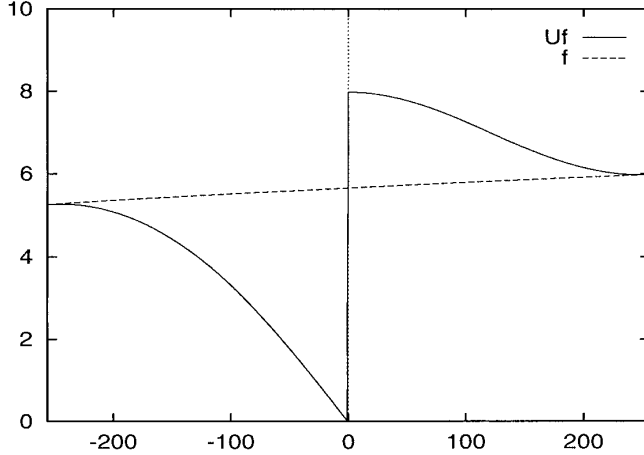


FIG. 5. Result of the folding operator.

$[a_n - \epsilon, a_{n+1} + \epsilon]$ into a smooth periodic function onto $[a_n, a_{n+1}]$, and expand it into the basis $\{e_{j,n}\}$. To do this we fold the overlapping parts of the window b_n and of the bump v back into the interval, across the endpoints of the interval, with some folding and unfolding operators. The advantage of the procedure is that we can preprocess the data with the folding operators and then use a conventional FFT to calculate the expansion into the basis $\{e_{j,n}\}$. We will follow the construction of Wickerhauser in [9].

A.1. Unitary Folding and Unfolding

We define the unitary folding operator U_{a_n} and its adjoint, the unfolding operator $U_{a_n}^*$, as follows:

$$U_{a_n}f(t) = \begin{cases} r\left(\frac{a_n - t}{\epsilon}\right)f(t) - r\left(\frac{t - a_n}{\epsilon}\right)f(2a_n - t), & \text{if } a_n - \epsilon < t < a_n, \\ r\left(\frac{t - a_n}{\epsilon}\right)f(t) + r\left(\frac{a_n - t}{\epsilon}\right)f(2a_n - t), & \text{if } a_n < t < a_n + \epsilon, \\ f(t), & \text{otherwise;} \end{cases} \quad (7)$$

$$U_{a_n}^*f(t) = \begin{cases} r\left(\frac{a_n - t}{\epsilon}\right)f(t) + r\left(\frac{t - a_n}{\epsilon}\right)f(2a_n - t), & \text{if } a_n - \epsilon < t < a_n, \\ r\left(\frac{t - a_n}{\epsilon}\right)f(t) - r\left(\frac{a_n - t}{\epsilon}\right)f(2a_n - t), & \text{if } a_n < t < a_n + \epsilon, \\ f(t), & \text{otherwise.} \end{cases} \quad (8)$$

Figures 5 and 6 show the result of the folding and unfolding operators.

We can then define the periodized folding and unfolding operators. These operators

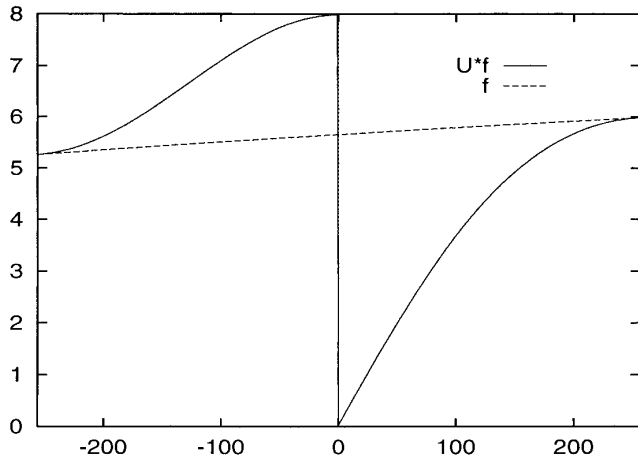


FIG. 6. Result of the unfolding operator.

fold and unfold the right end of the segment with the left end. The periodized folding operator $W_{a_n, a_{n+1}}$ and its adjoint $W_{a_n, a_{n+1}}^*$ are defined as follows:

$$W_{a_n, a_{n+1}} f(t) = \begin{cases} r\left(\frac{t - a_n}{\epsilon}\right)f(t) + r\left(\frac{a_n - t}{\epsilon}\right)f(a_n + a_{n+1} - t), & \text{if } a_n < t < a_n + \epsilon, \\ r\left(\frac{a_{n+1}\epsilon}{-} t\right)f(t) - r\left(\frac{t - a_{n+1}}{\epsilon}\right)f(a_n + a_{n+1} - t), & \text{if } a_{n+1} - \epsilon < t < a_{n+1}, \\ f(t), & \text{otherwise;} \end{cases} \quad (9)$$

$$W_{a_n, a_{n+1}}^* f(t) = \begin{cases} r\left(\frac{t - a_n}{\epsilon}\right)f(t) - r\left(\frac{a_n - t}{\epsilon}\right)f(a_n + a_{n+1} - t), & \text{if } a_n < t < a_n + \epsilon, \\ r\left(\frac{a_{n+1} - t}{\epsilon}\right)f(t) + r\left(\frac{t - a_{n+1}}{\epsilon}\right)f(a_n + a_{n+1} - t), & \text{if } a_{n+1} - \epsilon < t < a_{n+1}, \\ f(t), & \text{otherwise.} \end{cases} \quad (10)$$

Let $\mathbf{1}_{a_n, a_{n+1}}$ be the restriction operator:

$$\mathbf{1}_{a_n, a_{n+1}} f = \begin{cases} f(x), & \text{if } x \in [a_n, a_{n+1}] \\ 0, & \text{otherwise.} \end{cases} \quad (11)$$

Figures 7 and 8 show the result of the periodized folding and unfolding operators.

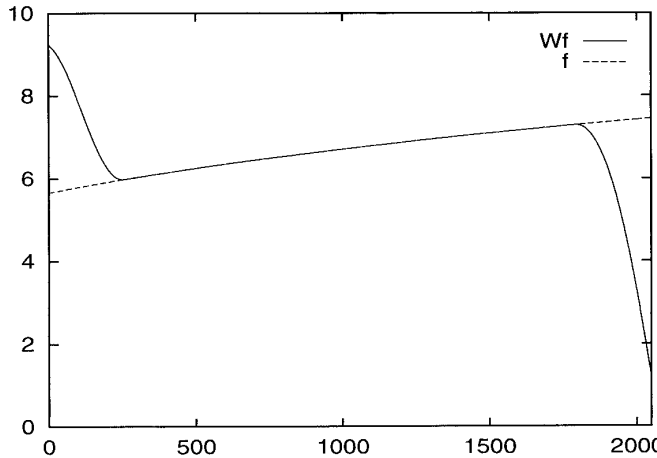


FIG. 7. Result of the periodized folding operator.

We can then use folding and unfolding to build an orthogonal transformation that restricts the function to an interval and periodizes the function while preserving smoothness. We define the *smooth periodic restriction operator* $T_{a_n, a_{n+1}}$ as follows:

$$T_{a_n, a_{n+1}} f = W_{a_n, a_{n+1}}^* \mathbf{1}_{a_n, a_{n+1}} U_{a_n} U_{a_{n+1}} f. \quad (12)$$

Let $T_{a_n, a_{n+1}}^*$ be the adjoint of $T_{a_n, a_{n+1}}$,

$$T_{a_n, a_{n+1}}^* f = U_{a_n}^* U_{a_{n+1}}^* \mathbf{1}_{a_n, a_{n+1}} W_{a_n, a_{n+1}} f. \quad (13)$$

A simple calculation shows that applying the operator $T_{a_n, a_{n+1}}^*$ to the basis $e_{j,n}$ gives us the basis $u_{j,n}$,

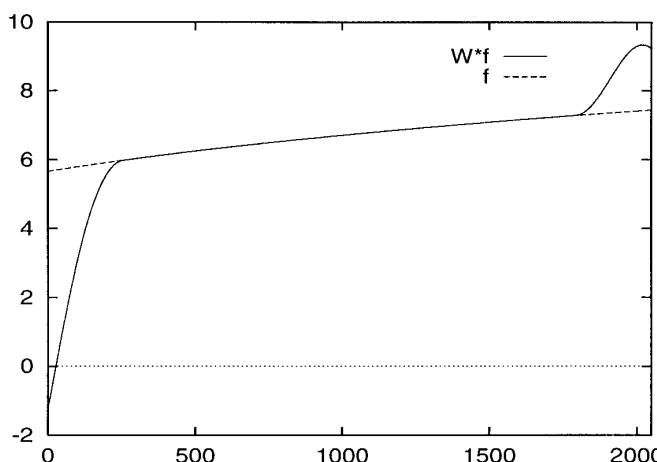


FIG. 8. Result of the periodized unfolding operator.

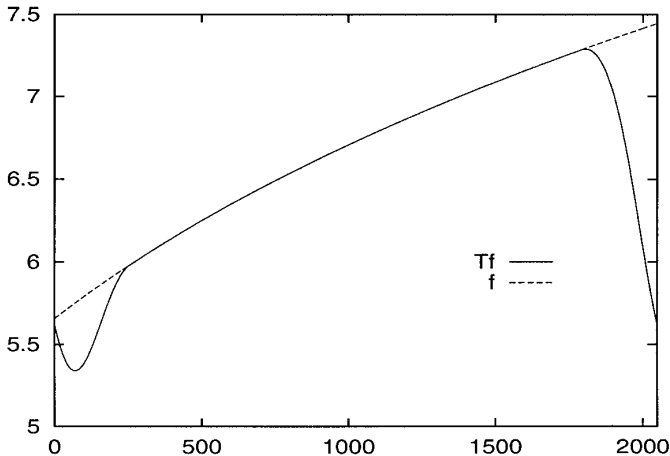


FIG. 9. Result of the smooth periodic restriction operator.

$$u_{j,n} = T_{a_n, a_{n+1}}^* e_{j,n}, \quad (14)$$

and we have

$$T_{a_n, a_{n+1}}^* T_{a_n, a_{n+1}} = U_{a_n}^* U_{a_{n+1}}^* \mathbf{1}_{a_n, a_{n+1}} U_{a_n} U_{a_{n+1}}. \quad (15)$$

We then have the following result [9]:

LEMMA 1. *The operators $P_{a_n, a_{n+1}} = T_{a_n, a_{n+1}}^* T_{a_n, a_{n+1}}$ are smooth orthogonal projectors.*

(i) $P_{a_n, a_{n+1}} + P_{a_{n+1}, a_{n+2}} = P_{a_n, a_{n+2}}$.

(ii) $L^2(\mathbb{R}) = \bigoplus_{n \in \mathbb{Z}} P_{a_n, a_{n+1}} L^2(\mathbb{R})$.

(ii) If $f \in C^d(\mathbb{R})$, then $P_{a_n, a_{n+1}} f$ has a unique continuous extension in $C^d(\mathbb{R})$ that is supported in the interval $[a_n - \epsilon, a_{n+1} + \epsilon]$.

Figures 9 and 10 show the result of the periodized folding and unfolding operators.

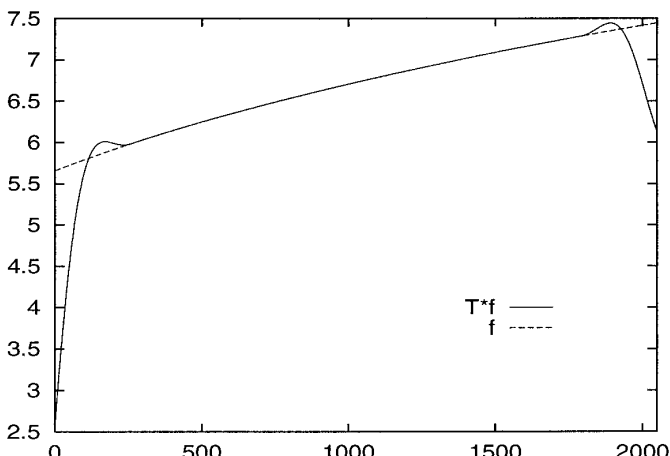


FIG. 10. Result of the adjoint of the smooth periodic restriction operator.

The coefficients $f_{j,n} = \langle f, u_{j,n} \rangle$ can then be calculated by expanding $T_{a_n, a_{n+1}} f$ into the basis $e_{j,n}$

$$\langle f, u_{j,n} \rangle = \langle f, T_{a_n, a_{n+1}}^* e_{j,n} \rangle = \langle T_{a_n, a_{n+1}} f, e_{j,n} \rangle. \quad (16)$$

To summarize, the correlation between f and $u_{j,n}$ is calculated as follows:

1. calculate $T_{a_n, a_{n+1}} f$ using the folding operator $T_{a_n, a_{n+1}}$,
2. expand $T_{a_n, a_{n+1}} f$ into $e_{j,n}$ using an FFT.

Conversely the reconstruction of f from $\langle f, u_{j,n} \rangle$ is done as follows:

1. recover $T_{a_n, a_{n+1}} f$ using an inverse FFT,
2. calculate the smooth orthogonal projection $P_{a_n, a_{n+1}} f = T_{a_n, a_{n+1}}^* T_{a_n, a_{n+1}} f$ using the folding operator $T_{a_n, a_{n+1}}^*$, and
3. add successive $P_{a_n, a_{n+1}} f$ to recover the complete signal $f = \sum_{n \in \mathbb{Z}} P_{a_n, a_{n+1}} f$.

B. Discrete Implementation of the Folding and Unfolding Operators

We assume that the original signal f has been sampled at N equally spaced mesh nodes. Let F_k be the value of the signal at node k

$$F_k = f(kh) \quad k = 0, 1, \dots, N - 1 \quad (17)$$

where h is the distance between two samples. We use a discrete ramp function r such that

$$r^2(t) + r^2(-t - 1) = 1. \quad (18)$$

In other words the discrete version of the folding operator will fold around the midpoint $-\frac{1}{2}$. We calculate the samples of the ramp function at the nodes $-dh, (-d + 1)h, \dots, 0, h, \dots, (d - 1)h$ where d is the smallest integer such that

$$\epsilon \leq dh. \quad (19)$$

We define

$$R_k = \begin{cases} 0 & \text{if } k < -d \\ r\left(\frac{k}{d}\right) & \text{if } k = -d, \dots, d \\ 1 & \text{otherwise.} \end{cases} \quad (20)$$

The discrete folding operator U_n modifies the sequence $(F_k)_{k \in \mathbb{Z}}$ around the mesh points $k = n - d, n - d + 1, \dots, n + d - 1$. U_n is defined as follows:

$$(U_n F)_k = \begin{cases} R_{n-k-1} F_k - R_{k-n} F_{2n-k-1}, & \text{if } n-d \leq k \leq n-1 \\ R_{k-n} F_k + R_{n-k-1} F_{2n-k-1} & \text{if } n \leq k \leq n+d-1 \\ F_k, & \text{otherwise.} \end{cases} \quad (21)$$

The discrete unfolding operator U_n^* is defined in a similar way. The discrete periodized folding and unfolding operators $W_{n,n+l-1}$ and $W_{n,n+l-1}^*$ are also defined in a similar way.

In order to apply the algorithm to a signal of finite length we usually make the sequence periodic: $F_{-1} = F_{N-1}$. It is also possible to extend the signal about both endpoints, 0 and $N-1$, for instance, symmetrically.

The discrete smooth periodic restriction operator $T_{n,n+l-1}$ is defined as a combination of the discrete folding and unfolding operators. For a sequence F , the smooth periodic restriction of F is defined as follows:

$$T_{n,n+l-1} F = W_{n,n+l-1}^* \mathbf{1}_{n,n+l-1} U_n U_{n+l-1} F. \quad (22)$$

Finally, we consider $E_{j,n}$ to be the discrete version of the basis $e_{j,n}$, defined as

$$E_{j,n}(k) = \frac{1}{\sqrt{l}} e^{-2i\pi j((k-n)/l)} \quad k = n, n+1, \dots, n+l-1 \quad (23)$$

for $j = 0, 1, \dots, l-1$.

In order to calculate the expansion of $T_{n,n+l-1} F$ into the basis $E_{j,n}$ we use an FFT.

III. BIORTHOGONAL WINDOWED FOURIER BASES

In Section V it will be desirable to build a basis of windowed exponentials with the constraint that the Fourier transform of the window, \hat{b}_n , is positive. However, this constraint and the constraint (3) are incompatible. Therefore, we will need to relax condition (3), and we will construct two biorthogonal windowed Fourier bases as explained in the following.

We construct here biorthogonal bases of smooth localized exponentials. One basis can be used for decomposition or analysis, and the other one for reconstruction, or synthesis. We will proceed in a way similar to [10].

We note that if we impose $\hat{b}_n(\xi) \geq 0$ then $b_n''(0) = \int (-2i\pi)^2 \hat{b}_n(\xi) d\xi < 0$ and the bell b_n cannot be flat in the center of the interval. Therefore we need to take $\epsilon = l_n/2$, and all intervals should have the same size $l = 2\epsilon$, and all the bells b_n will be the same.

We consider here a cover $\mathbb{R} = \bigcup_{n=-\infty}^{n=+\infty} [a_n, a_{n+1}]$, with $a_{n+1} - a_n = l$. Let $c_n = (a_n + a_{n+1})/2$. Let r be a ramp function such that

$$r(t) = 0 \quad \text{if } t \leq -1 \quad (24)$$

and

$$r^2(t) + r^2(-t) > 0, \quad \forall t \in \mathbb{R}. \quad (25)$$

Let v be the bump function supported on $[-l/2, l/2]$,

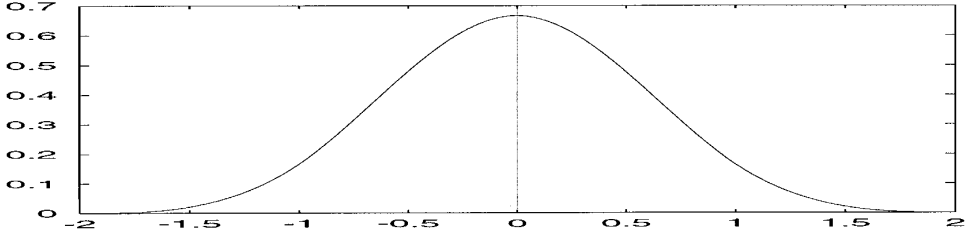


FIG. 11. Windowing function b , with $l = 2$.

$$v(t) = r\left(\frac{t}{l/2}\right)r\left(-\frac{t}{l/2}\right), \quad (26)$$

and let b be the windowing function supported on $[-l, l]$ (see Fig. 11).

$$\begin{aligned} b(t) &= r^2\left(\frac{t + l/2}{l/2}\right) && \text{if } t \in [-l, 0] \\ &= r^2\left(\frac{l/2 - t}{l/2}\right) && \text{if } t \in [0, l]. \end{aligned} \quad (27)$$

We choose r such that \hat{b} , the Fourier transform of b , is positive. An example of such b is the cubic spline

$$C(x) = \chi_{[-1/2, 1/2]} * \chi_{[-1/2, 1/2]} * \chi_{[-1/2, 1/2]} * \chi_{[-1/2, 1/2]}, \quad (28)$$

where $\chi_{[-1/2, 1/2]}$ is the characteristic function of $[-\frac{1}{2}, \frac{1}{2}]$. C is compactly supported on $[-2, 2]$, as shown in Fig. 11. Since the Fourier transform of $\chi_{[-1/2, 1/2]}$ is $\sin(\pi\xi)/\pi\xi$, the Fourier transform of C is

$$\hat{C}(\xi) = \left(\frac{\sin(\pi\xi)}{\pi\xi}\right)^4.$$

The tail of \hat{C} is rapidly decreasing to zero.

Another choice for b is the Gaussian. In theory, b is not compactly supported, but in practice we can select the parameters of the Gaussian so that the two Gaussians that live on $[a_n, a_{n+1}]$ and on $[a_{n+2}, a_{n+3}]$ do not overlap “numerically.” We note that our construction makes it possible for the two Gaussians that live on $[a_n, a_{n+1}]$ and on $[a_{n+1}, a_{n+2}]$ to overlap.

Let s be the l periodic function

$$s(x) = \frac{1}{\sum_{k \in \mathbb{Z}} r^2((x - a_k)/(l/2)) + r^2((a_k - x)/(l/2))}. \quad (29)$$

As above, we consider the collection of exponential functions

$$e_{j,n} = \frac{1}{\sqrt{l}} e^{-2i\pi j((x-a_n)/l)}.$$

First, we construct a basis of smooth localized orthonormal exponential functions $u_{j,n}$. Each $u_{j,n}$ is supported on $[a_n - l/2, a_{n+1} + l/2]$,

$$u_{j,n}(x) = b(x - c_n)e_{j,n}(x) + v(x - a_n)e_{j,n}(2a_n - x) - v(x - a_{n+1})e_{j,n}(2a_{n+1} - x). \quad (30)$$

Then the dual basis is defined as

$$\tilde{u}_{j,n}(x) = s^2(x)u_{j,n}(x). \quad (31)$$

We have the following result

LEMMA 2.

$$\int u_{j,n}(x)\tilde{u}_{k,m}(x)dx = \delta_{j,k}\delta_{n,m}. \quad (32)$$

$$\forall f \in L^2(\mathbb{R}),$$

$$f(x) = \sum_{j,n} f_{j,n} u_{j,n}(x) \quad \text{with } f_{j,n} = \int f(x)\tilde{u}_{j,n}(x)dx \quad (33)$$

$$f(x) = \sum_{j,n} \tilde{f}_{j,n} u_{j,n}(x) \quad \text{with } \tilde{f}_{j,n} = \int f(x)u_{j,n}(x)dx. \quad (34)$$

$u_{j,n}$ and $\tilde{u}_{j,n}$ are Riesz biorthogonal bases.

Proof. We first normalize the ramp function $r(t)$. Let

$$r^0(x) = \frac{r(x)}{\sqrt{r^2(x) + r^2(-x)}} \quad (35)$$

be the normalized ramp function that satisfies (3). We can then apply Theorem 1 and construct a local exponential basis u^0

$$u_{j,n}^0(x) = b^0(x - c_n)e_{j,n}(x) + v^0(x - a_n)e_{j,n}(2a_n - x) - v^0(x - a_{n+1})e_{j,n}(2a_{n+1} - x), \quad (36)$$

where $b^0(x)$ is the window function associated with r^0 defined by (5). Similarly, v^0 is the bump function associated with r^0 defined by (4).

If $x \in [a_n - l/2, a_n + l/2]$ then

$$\begin{aligned}
u_{j,n}^0(x) &= \frac{r^2((x - a_n)/(l/2))}{r^2((x - a_n)/(l/2)) + r^2((a_n - x)/(l/2))} e_{j,n}(x) \\
&\quad + \frac{r((x - a_n)/(l/2))r((a_n - x)/(l/2))}{r^2((x - a_n)/(l/2)) + r^2((a_n - x)/(l/2))} e_{j,n}(2a_n - x),
\end{aligned} \tag{37}$$

thus

$$u_{j,n}^0(x) = s(x) \left\{ r^2 \left(\frac{x - a_n}{l/2} \right) e_{j,n}(x) + r \left(\frac{x - a_n}{l/2} \right) r \left(\frac{a_n - x}{l/2} \right) e_{j,n}(2a_n - x) \right\} \tag{38}$$

and finally

$$u_{j,n}^0(x) = s(x) u_{j,n}(x). \tag{39}$$

Similarly, if $x \in [a_{n+1} - l/2, a_{n+1} + l/2]$ we get

$$u_{j,n}^0(x) = s(x) u_{j,n}(x). \tag{40}$$

We now use (39), (40), and the fact that $u_{j,n}^0$ is an orthonormal basis to prove (32). We have

$$\int u_{j,n}(x) \tilde{u}_{j,n}(x) dx = \int s^2(x) u_{j,n}(x) u_{j,n}(x) dx = \int u_{j,n}^0(x) u_{j,n}^0(x) dx = \delta_{j,k} \delta_{n,m}. \tag{41}$$

Let $f \in L^2(\mathbb{R})$; in order to prove (33), we expand $f(x)s(x)$ into the basis $u_{j,n}^0$. We have

$$f(x)s(x) = \sum_{j,n} \{fs\}_{j,n} u_{j,n}^0(x) = \sum_{j,n} \{fs\}_{j,n} u_{j,n}(x) s(x) \tag{42}$$

with

$$\{fs\}_{j,n} = \int f(x)s(x) u_{j,n}^0(x) dx = \int f(x)s^2(x) u_{j,n}(x) dx = \int f(x) \tilde{u}_{j,n}(x) dx. \tag{43}$$

Thus from (42) and (43) we obtain

$$f(x) = \sum \int f(x) \tilde{u}_{j,n}(x) dx u_{j,n}(x). \tag{44}$$

In a similar way, if we expand f/s into the basis $u_{j,n}^0$ we obtain (34). ■

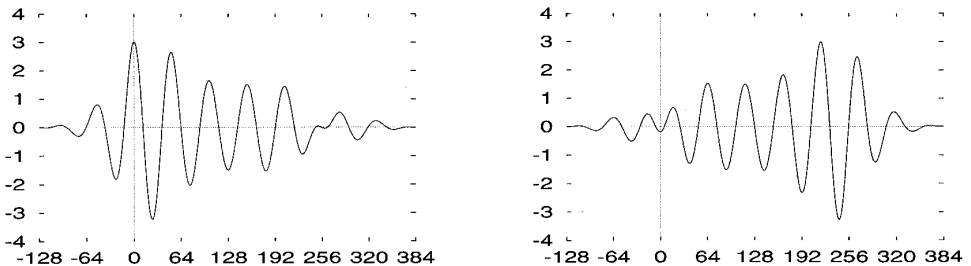


FIG. 12. Real (left) and imaginary (right) parts of the basis function $u_{j,n}$, with $a_n = 0$ and $a_{n+1} = 256$.

Figure 12 shows the real and imaginary part of the basis $u_{j,n}$. The basis was constructed using a cubic spline window. Figure 13 shows the real and imaginary part of the basis $\tilde{u}_{j,n}$. The graph of $\tilde{u}_{j,n}$ is really an exponential modulated by a cubic spline window.

A. Implementation by Folding

Rather than calculating the inner product $\langle f, u_{j,n} \rangle$, or $\langle f, \tilde{u}_{j,n} \rangle$, we can use the folding operators. The equations are the same as (7), (8) and (9), (10), except that now we need to use two different ramp functions for the analysis and the synthesis. The ramp function for the analysis is

$$\tilde{r}(t) = \frac{r(t)}{r^2(t) + r^2(-t)} \quad (45)$$

and the ramp function for the synthesis is $r(t)$.

Figure 14 shows a cubic spline window b , and Fig. 15 shows the dual window \tilde{b} . The analysis window \tilde{b} “magnifies” the value of the function on the border of the interval.

B. Discrete Implementation of the Folding and Unfolding Operators

The implementation of the folding and unfolding operators for the biorthogonal bases is the same as the implementation for the orthonormal bases. We should only pay attention to using a different ramp function for the analysis and for the synthesis.

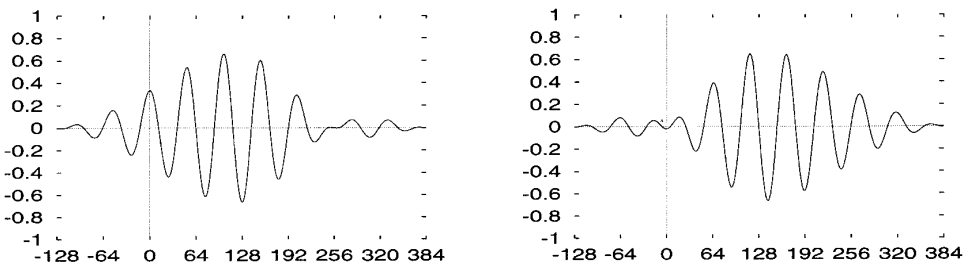


FIG. 13. Real (left) and imaginary (right) parts of the dual basis function $\tilde{u}_{j,n}$ with $a_n = 0$ and $a_{n+1} = 256$.

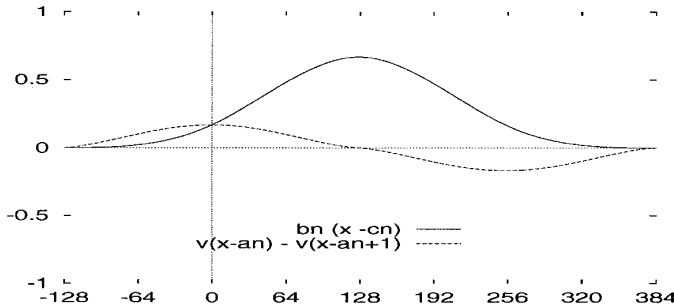


FIG. 14. Windowing function b_n (cubic spline) and bump function v at both ends of the interval.

IV. ORTHONORMAL BRUSHLET BASES

The orthonormal and biorthogonal windowed Fourier bases can be used to perform a time frequency analysis of an image. For a number of applications, it is more relevant to perform a time frequency analysis of the Fourier transform of the signal. This analysis corresponds to finding all the patterns in the image with a given orientation and frequency. In order to decompose the image into different oriented patterns we expand the Fourier transform into windowed Fourier bases. Our construction permits us to build a new set of reasonably well localized functions with only one peak in frequency.

A. One Dimensional Case

Let $f \in L^2(\mathbb{R})$, and let \hat{f} be the Fourier transform of f . We expand \hat{f} into the basis $u_{n,j}$,

$$\hat{f} = \sum \hat{f}_{n,j} u_{n,j}. \quad (46)$$

Then we take the inverse Fourier transform. Let $w_{n,j}$ the inverse Fourier transform of $u_{n,j}$.

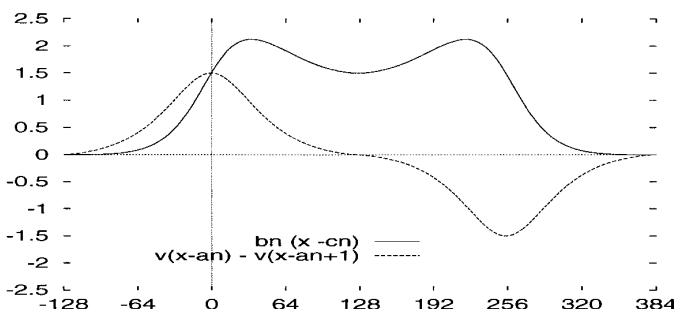


FIG. 15. Dual windowing function \hat{b}_n and dual bump function \hat{v} at both ends of the interval.

$$f = \sum \hat{f}_{n,j} w_{n,j} \quad (47)$$

Since the Fourier transform is a unitary operator, we obtain a new basis by applying the inverse Fourier transform on $u_{n,j}$:

LEMMA 3. $\{w_{n,j}, j, n \in \mathbb{Z}\}$ is an orthonormal basis for $L^2(\mathbb{R})$.

We call $\{w_{n,j}\}$ the orthonormal brushlet basis. From (6) we have

$$w_{n,j}(x) = \frac{1}{\sqrt{l_n}} e^{2i\pi c_n x} \left\{ (-1)^j \hat{b}_n \left(x - \frac{j}{l_n} \right) - 2i \sin(\pi l_n x) \hat{v} \left(x + \frac{j}{l_n} \right) \right\}. \quad (48)$$

We can introduce the “steepness factor” of the window b_n ,

$$\sigma = \frac{\epsilon}{l_n}. \quad (49)$$

We also introduce the window b_σ supported on $[-1/2 - \sigma, 1/2 + \sigma]$ such that

$$b_n(x) = b_\sigma \left(\frac{x}{l_n} \right), \quad (50)$$

and the bump function v_σ supported on $[-\sigma, \sigma]$ such that

$$v(x) = v_\sigma \left(\frac{x}{l_n} \right). \quad (51)$$

We have

$$\hat{b}_n(x) = l_n \hat{b}_\sigma(l_n x). \quad (52)$$

Then (48) can be rewritten as

$$w_{n,j}(x) = \frac{1}{\sqrt{l_n}} e^{2i\pi c_n x} \{ (-1)^j l_n \hat{b}_\sigma(l_n x - j) - 2i \sin(\pi l_n x) l_n \hat{v}_\sigma(l_n x + j) \}. \quad (53)$$

Then we have

$$w_{n,j}(x) = \sqrt{l_n} e^{2i\pi c_n x} e^{i\pi l_n x} \{ (-1)^j \hat{b}_\sigma(l_n x - j) - 2i \sin(\pi l_n x) \hat{v}_\sigma(l_n x + j) \}. \quad (54)$$

We note in (54) that l_n appears as a scaling factor of the analysis, and j is the translation index of the brushlet. $w_{n,j}$ has an expression similar to a wavelet. However, as opposed to a real valued wavelet, $w_{n,j}$ is a complex valued function with a phase. The phase encodes the orientation of the brushlet pattern in the two-dimensional case. b_σ and v_σ are even real-valued functions; thus \hat{b}_σ and \hat{v}_σ are also even real-valued functions.

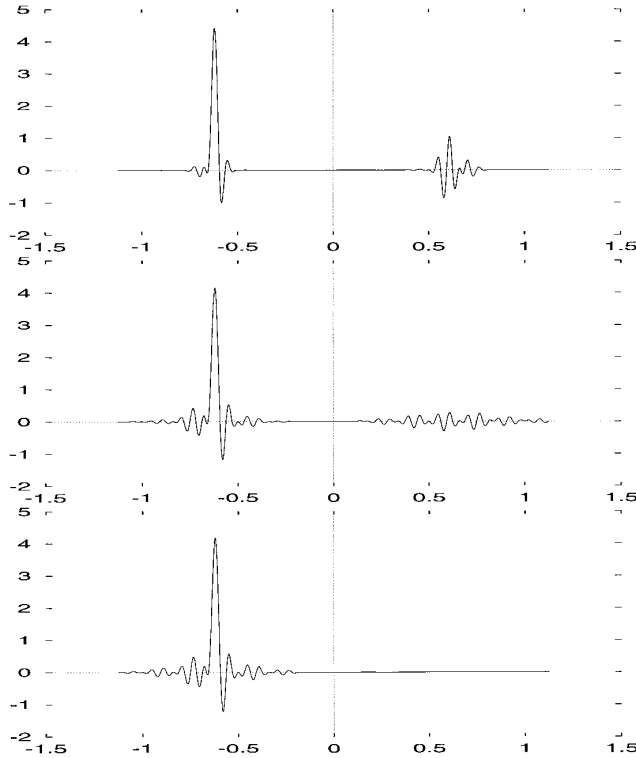


FIG. 16. Graph of the real part of $w_{n,j}$ on the interval for different values of ϵ , with $j/l_n = \frac{5}{8}$ and $a_n + l_n/2 = 3$. From top to bottom $\epsilon = 16$, $\epsilon = 4$, and $\epsilon = 0$. On the left is the principal part of the brushlet, a windowed exponential. On the right is the part necessary to obtain perfect localization in Fourier space. Note that when ϵ tends to zero, \hat{v} tends toward 0, but the principal part of the brushlet is less localized. When $\epsilon = 0$, the brushlet is the Shanon wavelet multiplied by an exponential.

The function $w_{n,j}$ is composed of two terms, localized around j/l_n and around $-j/l_n$, that are oscillating with the frequency $c_n = (a_n + a_{n+1})/2$. The first term is an exponential multiplied by the window \hat{b}_σ . Since $|\hat{v}_\sigma(x)| \leq \sigma$, the second term can be made as small as possible. However, when σ tends to zero the first term is not localized anymore. There is a tradeoff between the localization of \hat{b}_σ and the magnitude of the second term.

We choose σ such that the brushlet function is mainly localized around j/l_n . Figure 16 shows the graph of the real part of $w_{n,j}$ for a particular choice of r and for different values of σ .

B. Discrete Implementation of the Brushlet Expansion

We assume that the original signal f has been sampled at N equally spaced mesh nodes,

$$F_k = f(kh) \quad k = 0, 1, \dots, N-1. \quad (55)$$

First we calculate the Fourier transform of the discrete sequence F using an FFT. We obtain N samples,

$$\hat{F}_k = \hat{f}\left(\frac{k}{h}\right), \quad k = -\frac{N}{2}, -\frac{N}{2} + 1, \dots, 0, \dots, \frac{N}{2} - 1. \quad (56)$$

Then we consider a cover of the set of integers

$$\left\{-\frac{N}{2}, \dots, \frac{N}{2} - 1\right\} \quad (57)$$

into N/l intervals of size l . For each interval

$$\left[j \frac{1}{h}, (j + l - 1) \frac{1}{h}\right]$$

we expand \hat{F} into the discrete orthonormal windowed Fourier basis, as explained in Section III-B. First we calculate $T_{j,j+l-1}(\hat{F})$ using the discrete smooth periodic restriction operator. Then we expand $T_{j,j+l-1}(\hat{F})$ into the basis $E_{n,j}$ using an FFT of size l . On $[j/h, (j + l - 1)/h]$, \hat{F} is uniquely characterized by the samples at the mesh points

$$\frac{j}{h}, \dots, \frac{j + l - 1}{h}.$$

Since $T_{j,j+l-1}$ is a unitary isomorphism, $T_{j,j+l-1}(\hat{F})$ is also uniquely characterized by the samples

$$\frac{j}{h}, \dots, \frac{j + l - 1}{h}.$$

Finally, the discrete Fourier transform of $T_{j,j+l-1}(\hat{F})$ is characterized by the samples at the mesh points

$$0, \frac{h}{l}, \dots, h \frac{l-1}{l}.$$

Let $W_{n,j}$ be the discrete version of the basis function $w_{n,j}$. We note that even though the support of $W_{n,j}$ is larger than $[0, h(l-1)/l]$, $W_{n,j}$ is entirely characterized by the samples

$$0, \frac{h}{l}, \dots, h \frac{l-1}{l}.$$

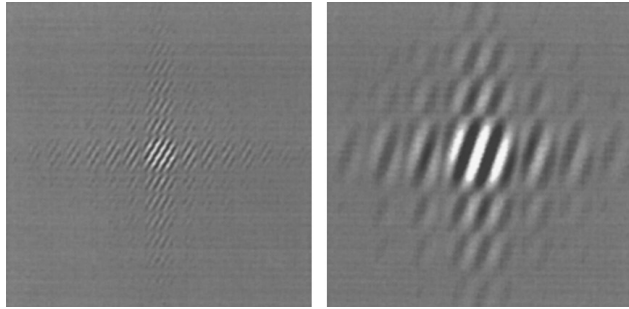


FIG. 17. Two-dimensional brushlet basis functions $\{w_{m,j} \otimes w_{n,k}\}$. A good spatial resolution corresponds to a \hat{b} with a small support and is thus associated with a poor frequency resolution as shown on the left. A good frequency resolution corresponds to a b with a small support and is thus associated with a poor spatial resolution as shown on the right.

This result is similar to the subsampling operation in multiresolution analysis. Here the subsampling is performed by selecting a subinterval of the global Fourier transform and expanding it into a local Fourier basis. In (54) we can replace x by the sample $k(h/l)$, $k = 0, \dots, l - 1$, and l_n by l/h , and we obtain the discrete version of $w_{n,j}$:

$$W_{n,j}(k) = \sqrt{l} e^{2i\pi(jk/l)} e^{i\pi k} \{(-1)^n \hat{b}_\sigma(k - n) - 2i \sin(\pi k) \hat{v}_\sigma(k + n)\},$$

$$k = 0, \dots, l - 1, \quad (58)$$

with

$$0 \leq n \leq l - 1.$$

C. Two-Dimensional Case

In the two-dimensional case we define two partitions of \mathbb{R} , $\cup_{j=-\infty}^{j=+\infty}[x_j, x_{j+1}[$ and $\cup_{k=-\infty}^{k=+\infty}[y_k, y_{k+1}[$.

We write $h_j = x_{j+1} - x_j$ and $l_k = y_{k+1} - y_k$. We then consider the tiling obtained by the lattice cubes $[x_j, x_{j+1}[\otimes [y_k, y_{k+1}[$. We consider the separable tensor products of bases $w_{m,j}$ and $w_{n,k}$. We have

LEMMA 4. *The sequence $w_{m,j} \otimes w_{n,k}$ is an orthonormal basis for $L^2(\mathbb{R}^2)$. ■*

C.1. Directional Image Analysis

We have

$$w_{m,j}(x) \otimes w_{n,k}(y) = \sqrt{h_j l_k} e^{2i\pi \frac{x_j+x_{j+1}}{2} x + \frac{y_k+y_{k+1}}{2} y}$$

$$\times \{(-1)^m \hat{b}_\sigma(h_j x - m) - 2i \sin(\pi h_j x) \hat{v}_\sigma(h_j x + m)\}$$

$$\times \{(-1)^n \hat{b}_\sigma(l_k y - n) - 2i \sin(\pi l_k y) \hat{v}_\sigma(l_k y + n)\}. \quad (59)$$

The tensor product $w_{m,j}(x) \otimes w_{n,k}(y)$ is an oriented pattern oscillating with the frequency $((x_j + x_{j+1})/2, (y_k + y_{k+1})/2)$ and localized at $(m/h_m, n/l_n)$, as shown in Fig. 17. The

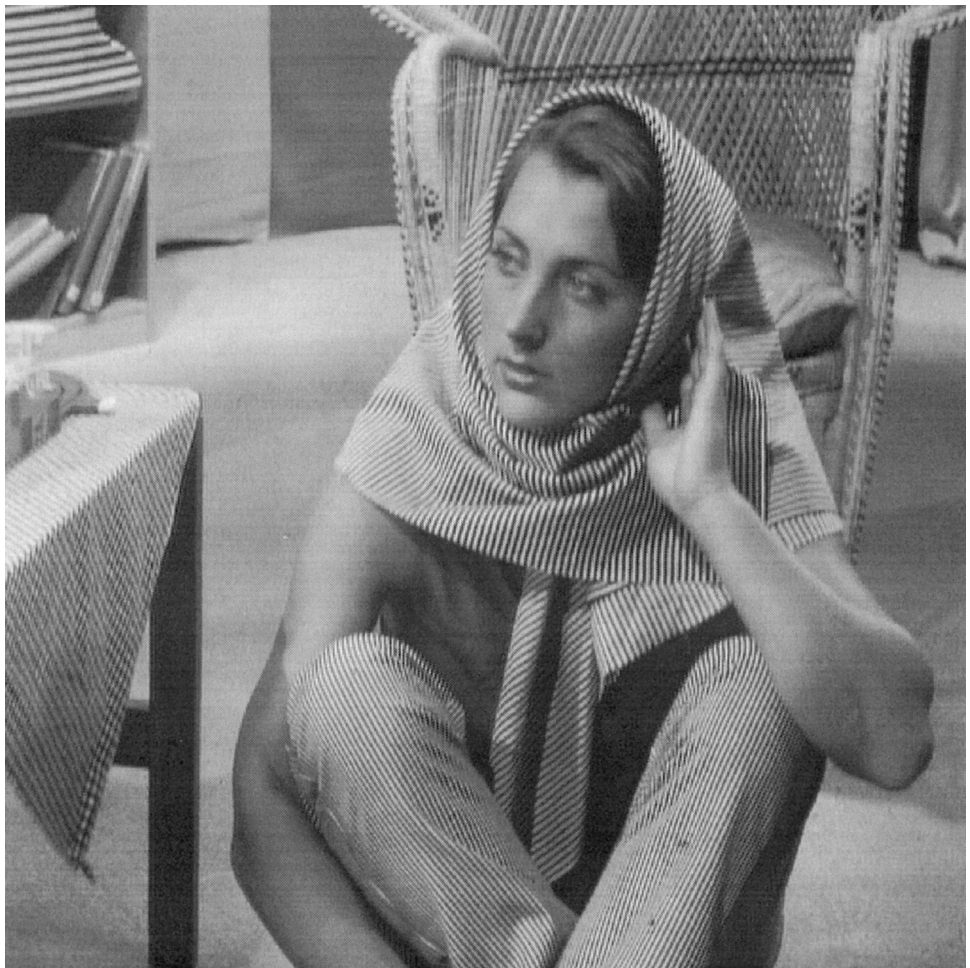


FIG. 18. Original 512×512 Barbara image.

size of the pattern is inversely proportional to the size of the analyzing window, $h_m \times l_n$ in the Fourier space.

The brushlet $w_{m,j}(x) \otimes w_{n,k}(y)$ is tuned to textures located at $(m/h_m, n/l_n)$ with a frequency $((x_j + x_{j+1})/2, (y_k + y_{k+1})/2)$. To illustrate the selective orientation analysis performed by the brushlet we have calculated the brushlet expansion of the image Barbara (shown in Fig. 18). A first expansion was performed with a portioning of the Fourier plane into four quadrants. We have $x_0 = -256$, $x_1 = 0$, $x_2 = 255$, and similarly $y_0 = -256$, $y_1 = 0$, $y_2 = 255$. The four sets of brushlets have the orientations $(\pi/4) + k(\pi/2)$, $k = 0, \dots, 3$. Figure 19 shows the imaginary part of the brushlets coefficients for each of the four quadrants of the Fourier plane. Since the signal is real, the coefficients are antisymmetric with respect to the origin. The upper right quadrant contains textures with patterns oriented along the direction $\pi/4$: the right leg, the mouth, the eyes, and the left arm. In the upper left window, textures with patterns oriented along the direction $3\pi/4$ are the left leg, the nose, and the right arm.

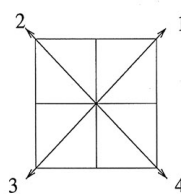
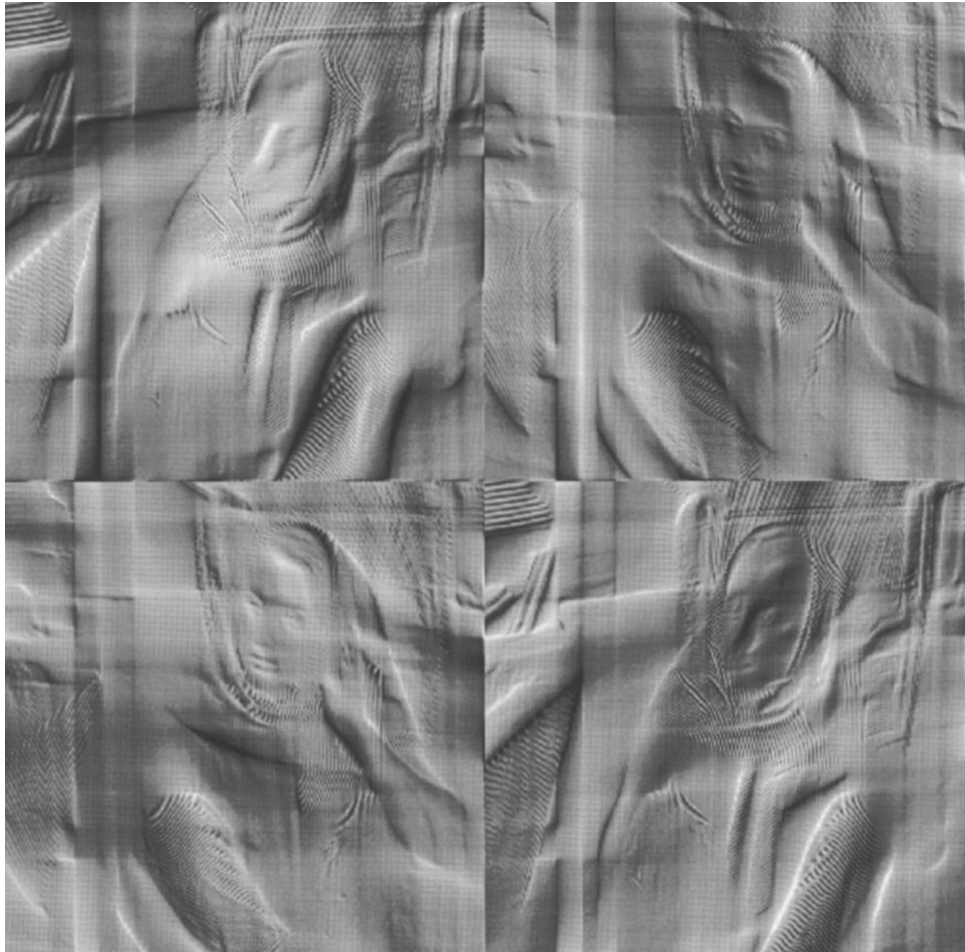


FIG. 19. Imaginary part of the brushlet coefficients for each of the four quadrants of the Fourier plane. Since the signal is real, the coefficients are antisymmetric with respect to the origin. The upper right quadrant contains textures with patterns oriented along the direction $\pi/4$: the right leg, the mouth, the eyes, and the left arm. In the upper left window, textures with patterns oriented along the direction $3\pi/4$ are shown: the left leg, the nose, and the right arm.

A second expansion has been performed using a finer grid. Each quadrant was further divided into four quadrants. The brushlet expansion was calculated for this finer tiling. The sixteen sets of brushlets have twelve different orientations as shown

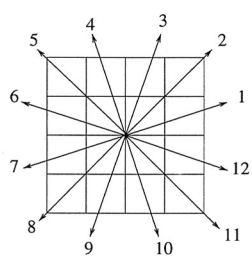
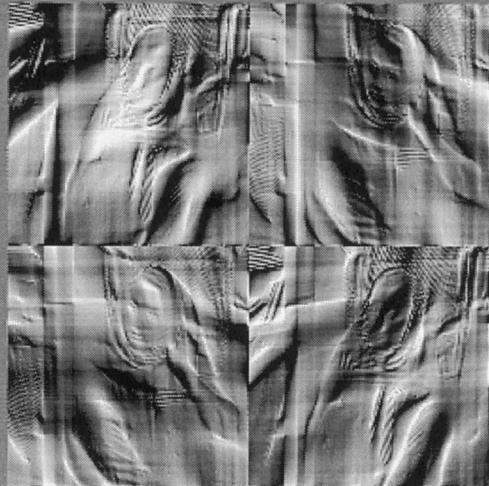


FIG. 20. Imaginary part of the brushlet expansion. The four lattice squares around the origin characterize the DC terms of the expansion. The other squares correspond to higher frequency textures. The textures of the legs and on the scarf have been completely removed from the four DC regions but are present in the regions that have the directions 1 and 12.

in Fig. 20. The orientations $(\pi/4) + k(\pi/2)$ are associated with two different frequencies. Figure 20 shows the imaginary part of the brushlet expansion. Again the coefficients are antisymmetric with respect to the origin. The four lattice squares around

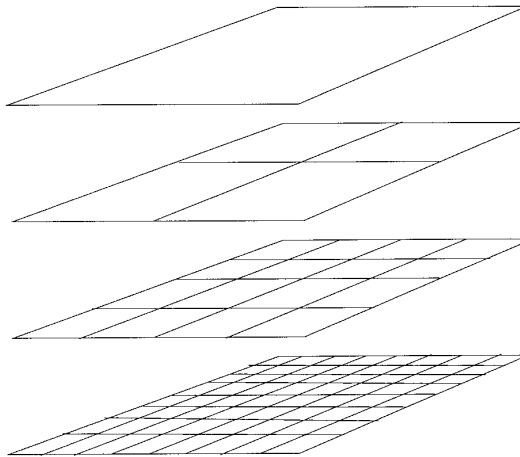


FIG. 21. Quadtree decomposition of the image. Within each block the image is expanded into a windowed Fourier transform. The optimal tiling is then searched for.

the origin characterize the DC terms of the expansion. The other squares correspond to higher frequency textures. We note that the texture of the legs and on the scarf have been completely removed from the four DC regions, but are present in the regions that have the directions 1 and 12 as shown in Fig. 20.

We note that the decomposition achieved by wavelet packets does not permit us to localize a unique frequency, for instance in the positive part of the Fourier space. Indeed, two symmetric windows are always associated with a real wavelet. As a result, a wavelet packet expansion will require many more coefficients to describe a pattern

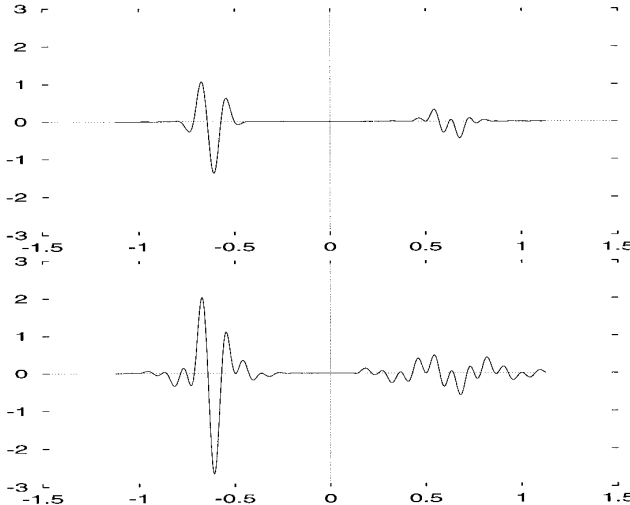


FIG. 22. (Top) Graph of the real part of the synthesis biorthogonal brushlet $\tilde{w}_{m,j}$, with $\epsilon = 4$, $j/l_n = \frac{5}{8}$, and $c_n = 7$. The biorthogonal brushlet is an exponential modulated by a cubic spline. (Down) Orthonormal brushlet $w_{m,j}$ with $\epsilon = 4$, $j/l_n = \frac{5}{8}$, and $c_n = 7$. The window of the orthonormal brushlet has many oscillations.

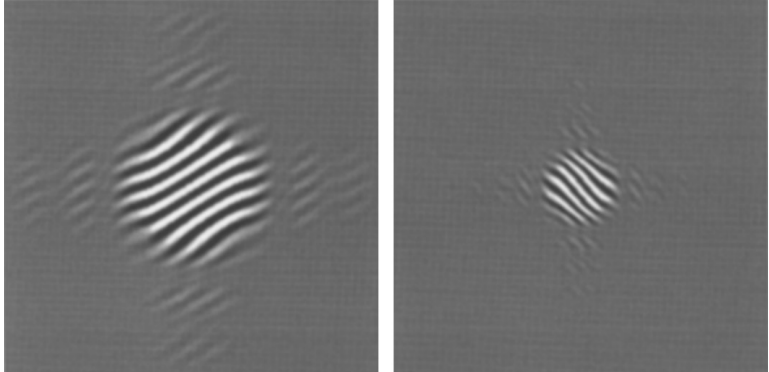


FIG. 23. Two-dimensional biorthogonal synthesis brushlet basis functions $\tilde{w}_{m,j} \otimes \tilde{w}_{n,k}$.

with an arbitrary orientation, whereas the same pattern can be coded with a single brushlet coefficient.

Directionally oriented filter banks (e.g., [11, 2]) have been used for image compression and image analysis. They do not allow, however, an arbitrary partitioning of the Fourier plane. Furthermore, in our method the tiling can be adapted to the image content, as explained in the next section.

D. Adaptive Tiling of the Fourier Plane

As explained in [9] we can adaptively select the size and location of the windows $[x_j, x_{j+1}[\otimes [y_k, y_{k+1}[$ with the best basis algorithm. We consider only tilings that can be generated from separable bases. We divide the Fourier plane into four subsquares, and we consider the brushlet basis associated with this tiling, as shown in Fig. 19. We then further decompose each square into four subsquares and consider the brushlet basis associated with this finer tiling, as shown in Fig. 20.

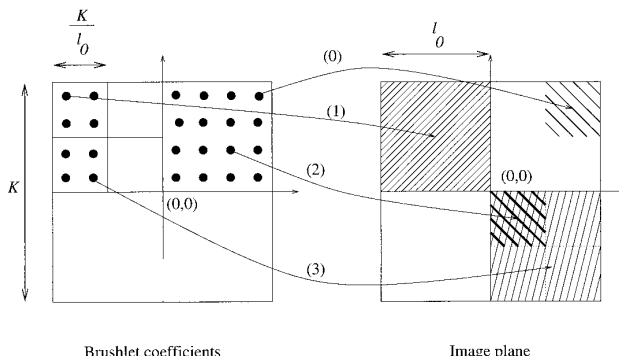


FIG. 24. Each pixel in a brushlet subblock corresponds to a subblock in the image plane. Conversely, each pixel in the image is decomposed into different brushlets. A good spatial resolution is associated with a poor frequency resolution as in (2). A good frequency resolution is associated with a poor spatial resolution as in (1) and (3). The best basis algorithm finds the optimal compromise between these two constraints with respect to the content of the image.

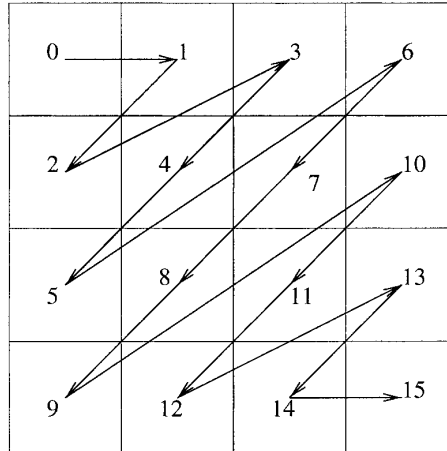


FIG. 25. Zigzag pattern that corresponds to ordering all the blocks in the frequency plane.

By applying this decomposition recursively, we obtain a homogeneous quadtree-structured decomposition as shown in Fig. 21. For each subblock, or node of the quadtree, we calculate the set of coefficients associated with the brushlets living on the subblock. If we associate a cost for each node of the tree, based on the set of coefficients, then we can find an optimal segmentation of the Fourier space. Using a divide and conquer algorithm, a group of four connected nodes are pruned if their total cost is greater than the cost of their father. The process is recursively applied from the bottom to the top of the quadtree, and a global optimal tree is then found.

(0,0)

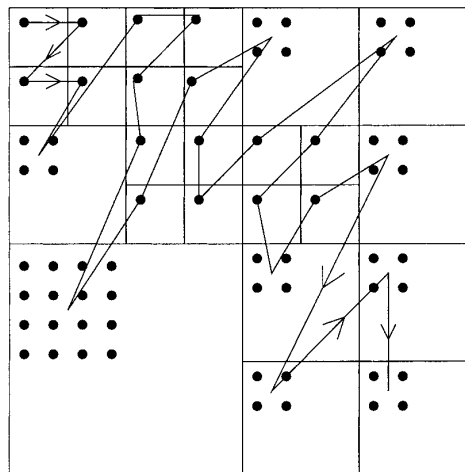


FIG. 26. We order by increasing frequency all the brushlet coefficients associated with the same region in the spatial domain. One coefficient in the upper left box (the smallest frequency) corresponds to a brushlet whose support is four times larger than the brushlets that correspond to the box in the lower right corner (largest frequency). For this reason we collect different numbers of coefficients inside each block.

TABLE 1
Coding Results for 8 bpp. 512 × 512 Lena

Compression rate	Brushlets: PSNR (dB)	EZW: PSNR (dB)
8	37.12	39.30
16	33.64	36.32
32	30.06	33.42
64	27.31	30.69
133	25.04	27.92
277	22.93	25.25
540	21.26	23.11

If we impose $\hat{b}_n \geq 0$, then we can construct biorthogonal windowed Fourier bases, as explained in Section III, and we are able to construct biorthogonal brushlet bases.

V. BIORTHOGONAL BRUSHLET BASES

We now construct biorthogonal brushlet bases. We first construct two biorthogonal trigonometric bases $\{u_{m,j}, \tilde{u}_{n,k}\}$ with a ramp function $r(x)$ such that the Fourier transform of b is positive. The support of $u_{m,j}$ is $[a_m - l/2, a_{m+1} + l/2]$. Let $w_{m,j}$ be the Fourier transform of $u_{m,j}$ and let $\tilde{w}_{n,k}$ be the Fourier transform of $\tilde{u}_{n,k}$. Since the Fourier transform is a unitary operator, we have

LEMMA 5. $\{w_{m,j}, \tilde{w}_{n,k}\}, k, m, n \in \mathbb{Z}\}$ are biorthogonal bases for $L^2(\mathbb{R})$.

We call $\{w_{m,j}, \tilde{w}_{n,k}\}$ the biorthogonal brushlet bases. We have

$$w_{m,j}(x) = \frac{1}{\sqrt{l}} e^{2i\pi c_m x} \left\{ (-1)^j \hat{b}\left(x - \frac{j}{l}\right) - 2i \sin(\pi l x) \hat{v}\left(x + \frac{j}{l}\right) \right\} \quad (60)$$

and the dual basis is given by

$$\tilde{w}_{n,k}(x) = \frac{1}{\sqrt{l}} e^{2i\pi c_n x} \left\{ (-1)^k \hat{b}\left(x - \frac{k}{l}\right) - 2i \sin(\pi l x) \hat{v}\left(x + \frac{k}{l}\right) \right\}, \quad (61)$$

TABLE 2
Coding Results for 8 bpp. 512 × 512 Barbara

Compression rate	Brushlets: PSNR (dB)	EZW: PSNR (dB)
8:1	35.16	35.60
16:1	30.51	30.16
32:1	24.95	26.73
65:1	23.39	24.71
127:1	21.63	23.23
271:1	20.45	22.29
592:1	19.28	21.05

TABLE 3
Coding Results for 8 bpp. 512 × 512 Mandrill

Compression rate	Brushlets: PSNR (dB)	EZW:PSNR (dB)
8	28.57	29.28
16	25.42	26.34
32	23.42	24.17
66	22.14	22.57
130	21.28	21.82
243	20.73	21.16

where \tilde{b} and \tilde{v} are the window and the bump functions associated with \tilde{r} , the dual ramp function defined in (45). Since \tilde{b} is a positive window the oscillation of the brushlet $w_{m,j}$ is only due to the exponential $e^{2i\pi c_n}$. Figure 22 shows the graph of the real part of $w_{m,j}$ when we use the cubic spline for b . For comparison purposes Fig. 22 also shows the graph of the real part of an orthonormal brushlet with the same parameters. We note that the biorthogonal brushlet is an exponential modulated by a cubic spline, while the window of the orthonormal brushlet has many oscillations.

A. Two-Dimensional Case

In a way similar to the orthonormal brushlets, we consider separable tensor products of bases. We have

LEMMA 6. *The sequences $w_{m,j} \otimes w_{n,k}$, $\tilde{w}_{p,q} \otimes \tilde{w}_{r,s}$ are biorthogonal bases for $L^2(\mathbb{R}^2)$.*

We use the synthesis brushlet $w_{m,j} \otimes w_{n,k}$, which has a positive window, to reconstruct the image. Figure 23 shows the pattern associated with the synthesis brushlet. We reconstruct the image with such localized oscillating patterns.

TABLE 4
Coding Results for 8 bpp. 512 × 512 Fingerprints

Compression rate	Brushlets: PSNR (dB)	EZW: PSNR (dB)
8	33.24	35.30
16	29.33	30.46
32	26.42	26.72
65	24.18	23.73
128	22.49	21.80
242	21.12	20.83
528	18.99	20.09



FIG. 27. Original 512×512 Lena image.

VI. IMAGE COMPRESSION

We have developed a coding algorithm that exploits an orthogonal brushlet expansion of the image.

A. Adaptive Multiresolution Brushlet Decomposition

The Fourier transform \hat{F} of the image f is computed using an FFT. \hat{F} is hermitian-symmetric, therefore we only retain the upper half of the Fourier plane $\{(\nu, \xi), \xi \geq 0\}$ for coding. We divide the upper half into two quadrants. For each quadrant the brushlet coefficients are calculated at different resolutions. Instead of calculating the inner product of \hat{F} with $u_{m,j} \otimes u_{n,k}$, we fold the image around the horizontal and vertical lines associated with the tiling as explained in Section II.A. We then calculate inside each block the 2D FFT of the folded



FIG. 28. Lena picture at a compression of 133:1 with brushlets, PSNR = 25.04 dB.

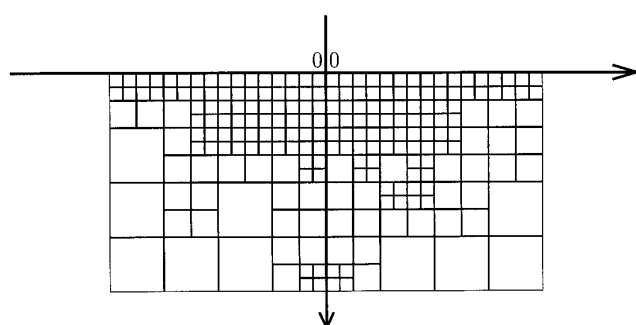


FIG. 29. Lena at a compression of 133:1 with brushlets: optimal tiling of the Fourier plane. The horizontal axis points toward the right, and the vertical axis points downward.



FIG. 30. Lena at a compression of 133:1 with EZW, PSNR = 27.92 dB.

block and obtain the brushlet coefficients. Finally, we estimate the optimal tiling of the brushlet bases at different resolutions using the best basis algorithm as explained in Section IV.C. Each block associated with the segmentation corresponds to a set of brushlet coefficients. These coefficients describe the intensity of one single “brush stroke” at different locations in the image, as illustrated in Fig. 24. This “brush stroke” has a particular frequency, orientation, and size that are given by the position of the block and its size.

B. Zig-Zag Scanning of the Coefficients

For both quadrants of the upper half of the Fourier plane we calculate the optimal segmentation using the local Fourier bases. This optimal segmentation corresponds to the optimal brushlet basis. Let $K/l_0 \times K/l_0$ be the size of the smallest block in the Fourier domain. This block corresponds to the brushlet with the largest support in the



FIG. 31. Barbara at a compression of 127:1, PSNR = 21.63 dB.

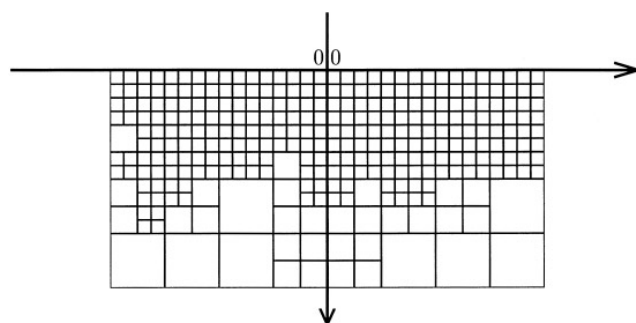


FIG. 32. Barbara at a compression of 127:1: optimal tiling of the upper half of the Fourier plane; the horizontal axis points toward the right and the vertical axis points downward.

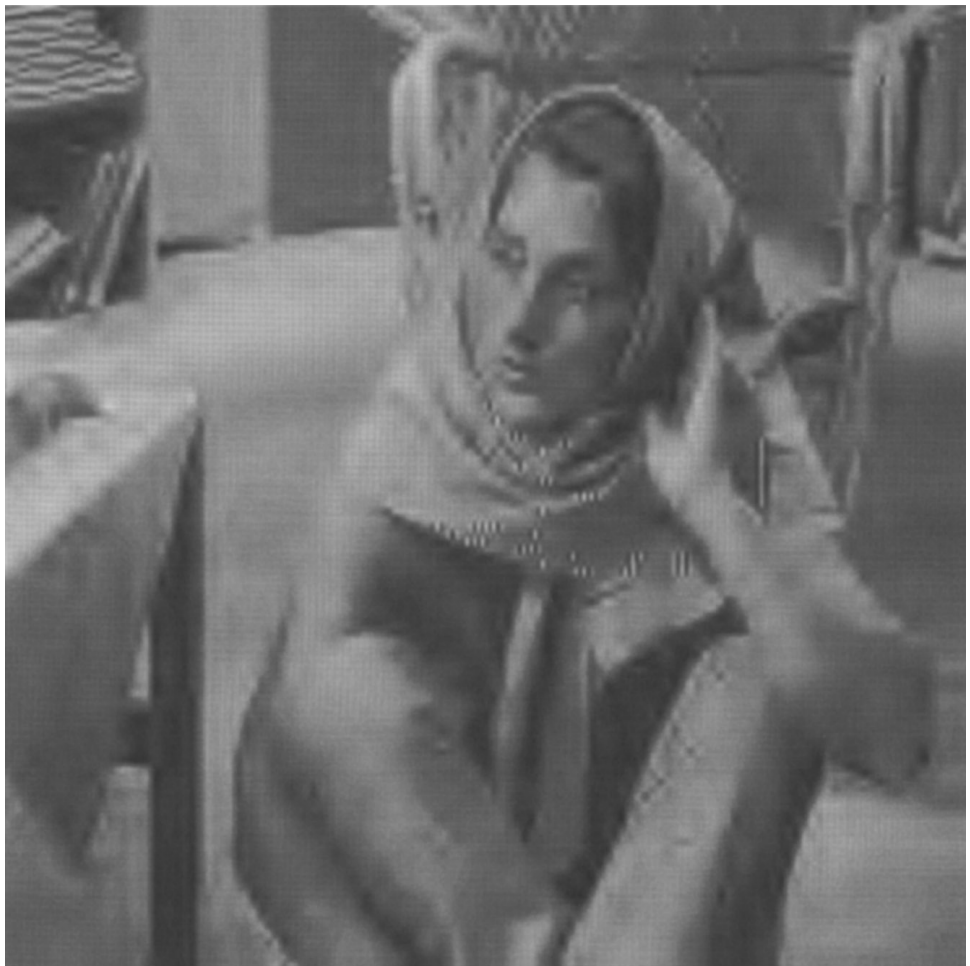


FIG. 33. Barbara at a compression of 127:1 with EZW, PSNR = 23.23 dB.

spatial domain as shown in Fig. 24. We then divide the $N \times N$ image F into $(N/l_0) \times (N/l_0)$ blocks of size $l_0 \times l_0$. For each of these image blocks, we gather all the coefficients of the brushlets which have their support in this block.

We start with the brushlet of smallest frequency and continue to the brushlet of highest frequency. The frequency of the brushlet is given by the center of the support of the brushlet in the Fourier domain (the center of the block in the Fourier domain). We define an order in the frequency plane as follows:

The frequency (ν_x^2, ν_y^2) is larger than the frequency (ν_x^1, ν_y^1) if

$$|\nu_x^1| + |\nu_y^1| < |\nu_x^2| + |\nu_y^2|$$

or

$$|\nu_x^1| + |\nu_y^1| = |\nu_x^2| + |\nu_y^2| \quad \text{and} \quad |\nu_y^1| < |\nu_y^2|. \quad (62)$$

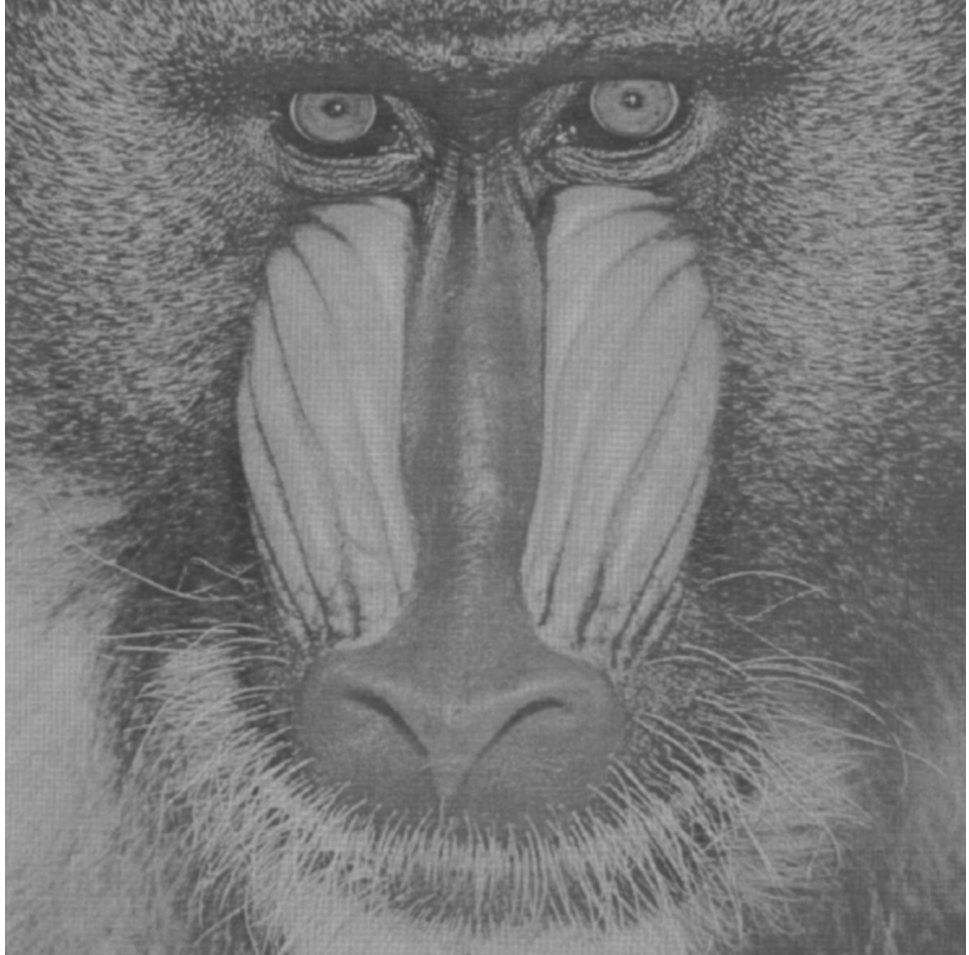


FIG. 34. Original 512×512 Mandrill image.

Figure 25 shows the zigzag patterns that correspond to ordering all the blocks in the frequency plane.

In practice, we order the coefficients by increasing frequency directly in the frequency plane. First we order the blocks using the order defined in (62). Then we search for the smallest block; the smallest block corresponds to the brushlet with the largest support. Each coefficient in the smallest block corresponds to a region in the image of size $l_0 \times l_0$.

We then create $(N/l_0) \times (N/l_0)$ sequences of coefficients. Each sequence gives the brushlet decomposition of a particular region of size $l_0 \times l_0$ in the image, as shown in Fig. 24. A sequence is created by scanning each block in the frequency domain by increasing frequency: inside each block we take all the coefficients of the basis functions that live in the particular region in the spatial domain. The algorithm is illustrated in Fig. 26.

The magnitude of the terms in each sequence decreases with an exponential decay.

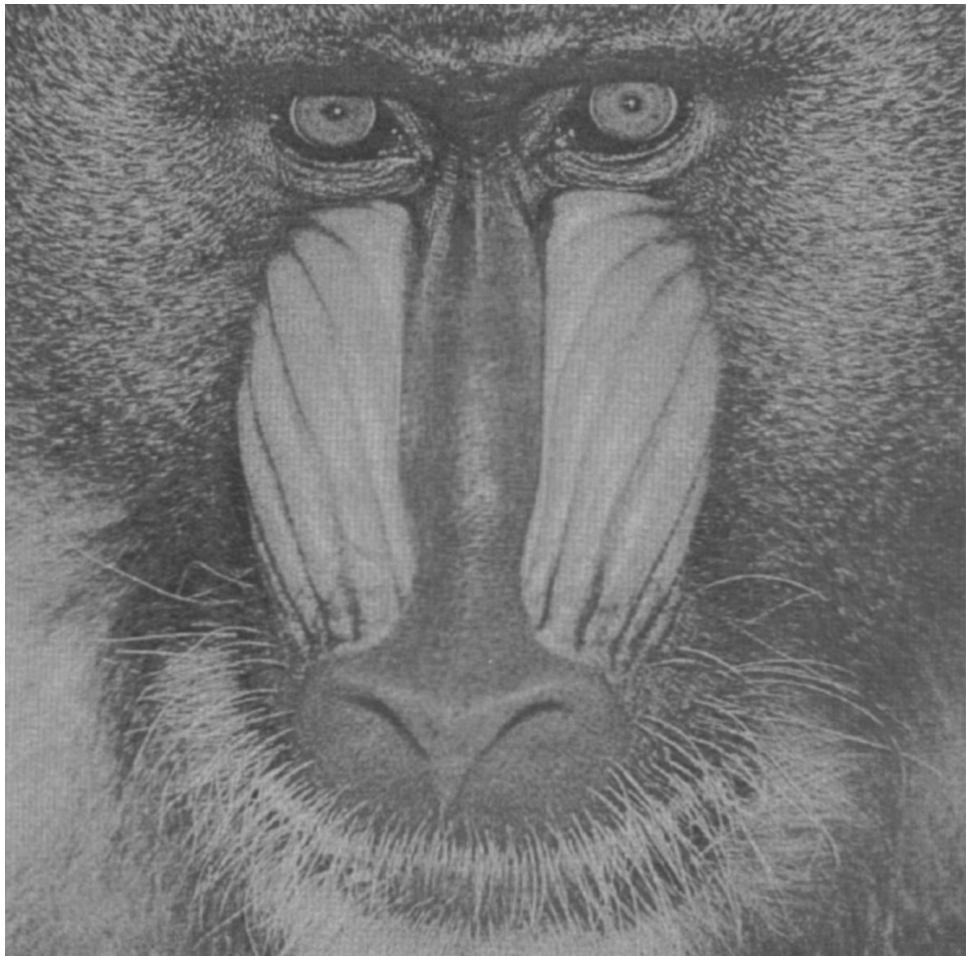


FIG. 35. Mandrill at a compression of 8:1 with brushlets, PSNR = 28.57 dB.

We exploit this property and we encode a terminating symbol after the last non-zero coefficient to indicate that the remaining coefficients are zeros. This represents a zero-tree-like extension of the algorithm proposed in [12].

C. Quantization of the Coefficients

After zig-zag ordering the coefficients are quantized. This is the stage where the compression becomes lossy. The brushlet coefficients are quantized with uniform quantizers.

D. Entropy Coding

After zig-zag ordering, the coefficients are then coded using variable length coding. The alphabet that describes the variable length encoding is entropy coded with an adaptive arithmetic coder [13]. The first term of a zig-zag scan corre-

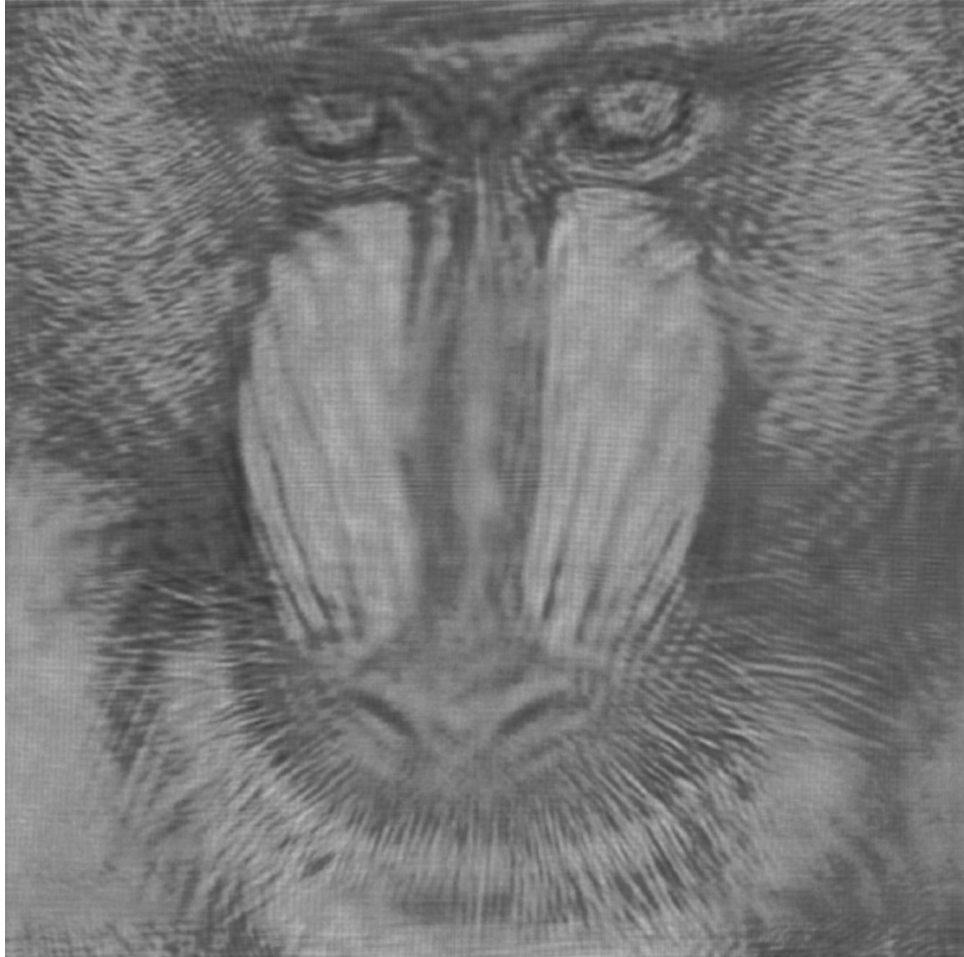


FIG. 36. Mandrill at a compression of 130:1 with brushlets, PSNR = 21.28 dB.

sponds to a DC coefficient. The DC coefficients of adjacent spatial locations are still correlated, as shown in Fig. 20, and are therefore differentially encoded.

We have implemented the coder and decoder, and an actual bit stream was created for each experiment.

E. Complexity

Our particular implementation of the method exploits the FFT. However, all calculations could be performed in the spatial domain; we would only need to calculate the coefficients of the filters associated with the operators defined in the Fourier domain. The compression algorithm would then achieve a complexity similar to the best basis decomposition using wavelet packets. Currently it takes 5 seconds to compress the 512×512 Mandrill image on a SGI workstation.

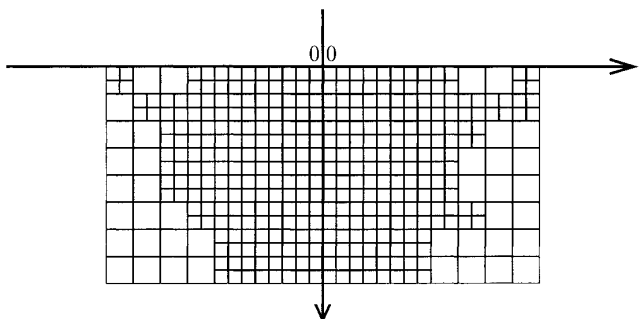


FIG. 37. Mandrill at a compression of 130:1 with brushlets: optimal tiling of the Fourier plane. The horizontal axis points toward the right, and the vertical axis points downwards.



FIG. 38. Mandrill at a compression of 130:1 with EZW, PSNR = 21.82 dB.



FIG. 39. Original 512×512 fingerprints image.

VII. EXPERIMENTS

We present the results of the algorithm using three test images: 512×512 ‘‘Lena,’’ 512×512 ‘‘Barbara,’’ and 512×512 ‘‘Mandrill.’’ Barbara and Mandrill are difficult to compress because they contain richly textured regions. The performance of the algorithm is summarized in Tables I–IV. We use the L^2 error to evaluate the quality of the compressed image. We define the mean squared error, D , between the $N \times N$ original image I and the compressed image I_c as

$$D = \frac{1}{N^2} \sum_{i,j=0}^{N-1} |I(i, j) - I_c(i, j)|^2. \quad (63)$$

We work with 8-bit images, and we define the peak signal-to-noise ratio (PSNR) of the compressed image as

$$\text{PSNR} = 10 \log_{10} \frac{255^2}{D}. \quad (64)$$



FIG. 40. Fingerprints at a compression of 128:1 with brushlets, PSNR = 22.49 dB.

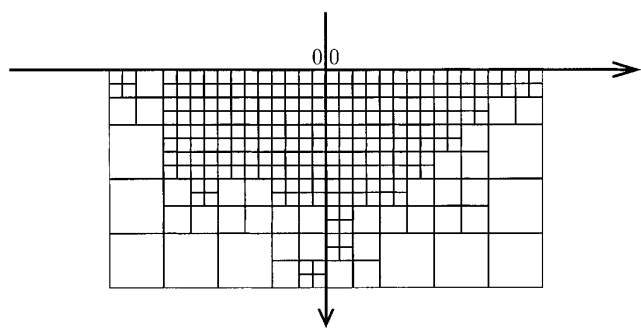


FIG. 41. Fingerprint at a compression of 128:1 with brushlets, and optimal tiling of the Fourier plane. The horizontal axis points toward the right, and the vertical axis points downward.

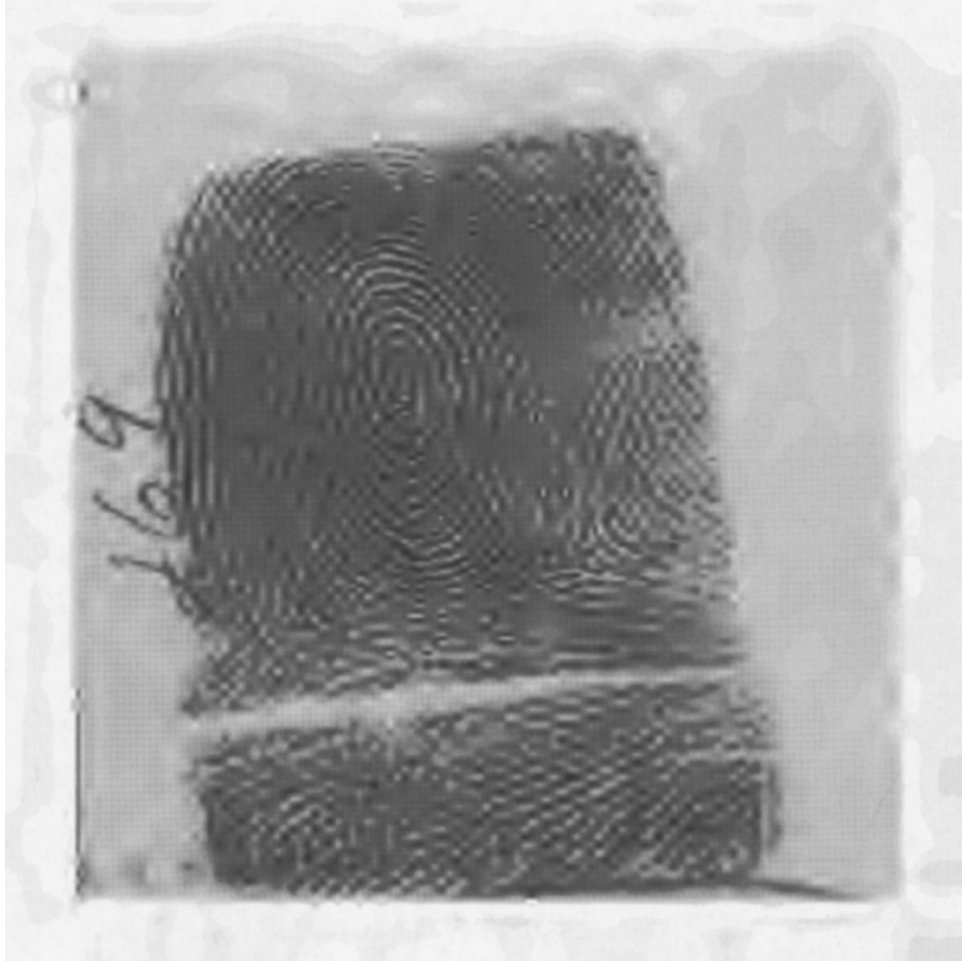


FIG. 42. Fingerprints at a compression of 128:1 with EZW, PSNR = 21.80 dB.

In order to emphasize the performance of the algorithm, we have used the EZW algorithm of Shapiro [12] to compress all images.

Figure 27 shows the original Lena image. Figure 28 shows the image Lena coded with brushlets at a compression ratio of 133:1. Figure 29 shows the optimal tiling of the upper half of the Fourier plane. Figure 30 shows the result of the compression with EZW at a compression ratio of 133. We note that the stripes on the hat and the texture on the fur have been kept intact with the brushlets, while they have been smeared with the wavelets.

Figure 18 shows the original Barbara image. Figure 31 shows the image Barbara coded with brushlets at a compression ratio of 127:1. Figure 32 shows the optimal tiling of the upper half of the Fourier plane. We note that the segmentation is not symmetric, reflecting some significant oriented textures in the image. Figure 33 shows the result of the compression with EZW at a compression ratio of 127. We note that the texture on the chair is very well preserved with the brushlets. It is clear from

these two experiments that a combination of brushlets and wavelets is needed to obtain even better results. We are currently working on this problem.

Figure 34 shows the original Mandrill image. Figure 35 shows the Mandrill image coded with brushlets at a compression ratio of 8:1, with a PSNR = 28.57 dB. We note that it is impossible to see the difference between the original and the compressed images. Figure 36 shows the Mandrill image coded with brushlets at a compression ratio of 130:1, with a PSNR = 21.28 dB. Figure 37 shows the optimal tiling of the upper half of the Fourier plane. Again we note that the segmentation is not symmetric. We also note that even at a compression ratio of 130:1 the Mandrill still keeps its high frequency features such as the whiskers. Figure 38 shows the image Mandrill coded with EZW at compression ratio of 130:1, with a PSNR = 21.82. We note that all the high frequency features such as the whiskers have been smeared.

Finally, we have evaluated our algorithm with a fingerprints image. Figure 39 shows the original fingerprint. Figure 42 shows the result of the compression with EZW at a compression ration of 128:1, with a PSNR = 21.80 dB. Figure 40 shows the result of the compression with our algorithm at a compression ration of 128:1, with a PSNR = 22.49 dB. The associated tiling of the Fourier plane is shown in Fig. 41. We note that most of the details have been smeared by EZW, while our algorithm keeps the structure of the fingerprint with a better PSNR.

VIII. CONCLUSION

We have addressed the problem of describing an image with a library of orthonormal, or biorthogonal, oriented patterns. We have proposed a new library of functions, called brushlets. The brushlets are oscillating functions reasonably well localized with only one peak in frequency. We have developed a compression algorithm that exploits this basis to obtain the most economical representation of the image in terms of textured patterns with different orientations, frequencies, sizes, and positions. The method has been carefully evaluated with different test images. We have shown that our compression algorithm has potential applications for compression of highly textured images. We are currently working on a texture segmentation method that exploits brushlets bases.

REFERENCES

1. K. Ramchandran and M. Vetterli, Best wavelet packet bases in a rate-distortion sense, *IEEE Trans. Image Process.* (Apr 1993), 160–175.
2. R. H. Bamberger and M. J. T. Smith, A filter bank for the directional decomposition of images: theory and design, *IEEE Trans. Signal Process.* (Apr 1992), 882–893.
3. W. T. Freeman and E. H. Adelson, The design and use of steerable filters, *IEEE Trans. Pattern Anal. Mach. Intell.* **13**, No. 9 (Sep 1991), 891–906.
4. M. V. Wickerhauser, Smooth localized orthonormal bases, *C. R. Acad. Sci. Paris I* (1993), 423–427.
5. I. Daubechies, “Ten Lectures on Wavelets,” SIAM, Philadelphia, 1992.
6. I. Daubechies, S. Jaffard, and J. L. Journé, A simple Wilson orthonormal basis with exponential decay, *SIAM J. Math. Anal.* **22** (1991), 554–572.

7. H. Malvar, Lapped transforms for efficient transform/subband coding, *IEEE Trans. Acoust. Sign. Speech Process.* **38** (1990), 969–978.
8. R. R. Coifman and Y. Meyer, Remarques sur l’analyse de Fourier à fenêtre, *C. R. Acad. Sci. Paris I* (1991), 259–261.
9. P. Auscher, G. Weiss, and M. V. Wickerhauser, Local sine and cosine bases of Coifman and Meyer and the construction of smooth wavelets, in ‘‘Wavelets—A Tutorial in Theory and Applications’’ (C. K. Chui, Ed.), Wavelet Analysis and Its Applications Series, Vol. 2, pp. 237–256, Academic Press, San Diego, 1992.
10. G. Matviyenko, ‘‘Optimized Local Trigonometric Bases, Res. Rep. YALEDU/DCS/RR-1041, Department of Computer Science, Yale University, 1994.
11. E. P. Simoncelli and E. H. Adelson, Nonseparable extensions of quadrature mirror filters to multiple dimensions, *Proc. IEEE*, (Apr 1990), 652–664.
12. J. M. Shapiro, Embedded image coding using zerotrees of wavelet coefficients, *IEEE Trans. Signal Process.* (Dec. 1993), 3445–3462.
13. I. H. Witten, R. M. Neal, and J. G. Cleary, Arithmetic coding for data compression, *Comm. ACM* **30**, No. 6 (June 1987), 520–540.